

Bifurcation and chaos in zero-Prandtl-number convection

P. PAL^{1(a)}, P. WAHI², S. PAUL¹, M. K. VERMA^{1(b)}, K. KUMAR³ and P. K. MISHRA¹

¹ *Department of Physics, Indian Institute of Technology - Kanpur, India*

² *Department of Mechanical Engineering, Indian Institute of Technology - Kanpur, India*

³ *Department of Physics and Meteorology, Indian Institute of Technology - Kharagpur, India*

received 1 June 2009; accepted in final form 21 August 2009

published online 22 September 2009

PACS 47.20.Bp – Buoyancy-driven instabilities (*e.g.*, Rayleigh-Bénard)

PACS 47.20.Ky – Nonlinearity, bifurcation, and symmetry breaking

PACS 47.27.ed – Dynamical systems approaches

Abstract – We present a detailed bifurcation structure and associated flow patterns near the onset of zero-Prandtl-number Rayleigh-Bénard convection. We employ both direct numerical simulation and a low-dimensional model ensuring qualitative agreement between the two. Various flow patterns originate from a stationary square observed at a higher Rayleigh number through a series of bifurcations starting from a pitchfork followed by a Hopf and finally a homoclinic bifurcation as the Rayleigh number is reduced to the critical value. Homoclinic chaos, intermittency, and crises are observed near the onset.

Copyright © EPLA, 2009

Thermal convection is observed almost everywhere in the universe: industrial appliances, liquid metals, atmosphere, oceans, interiors of planets and stars, galaxies etc. An idealized version of convection called Rayleigh-Bénard convection (RBC) has been studied for almost a century and it is still an area of intense research [1]. The two most important parameters characterizing convection in RBC are the Rayleigh number, describing the vigour of buoyancy, and the Prandtl number, being the ratio of kinetic viscosity and thermal diffusivity. Solar [2] and geological flows [3] are considered to have very low Prandtl numbers, as do flows of liquid metals [4]. RBC exhibits a wide range of phenomena including instabilities, patterns, chaos, spatio-temporal chaos, and turbulence for different ranges of Rayleigh number and Prandtl number [1]. The origin of instabilities, chaos, and turbulence in convection is one of the major research topics of convection.

Direct numerical simulation (DNS), due to its high dimensionality, generates realistic but excessively voluminous numerical outputs which obscure the underlying dynamics. Lower-dimensional projections lead to models which, if done improperly, lose the overall physics. In this letter, our aim is to unfold and discover the underlying physics of low-Prandtl-number flows [5] by examining the natural limit of zero Prandtl number (zero-P) [6–12]. This offers a dramatic simplification without sacrificing

significant physics, as well as displays a fascinatingly rich dynamic behaviour. In particular, since zero-P flows are chaotic immediately upon initiation of convection, we adopt a nonstandard strategy of approaching this system from the post-bifurcation direction. Moreover, we attack the problem simultaneously with DNS (to ensure accuracy) as well as a low-dimensional model (to aid physical interpretation); and we stringently refine both the model and DNS until satisfactory agreement is obtained at all levels of observed behaviour. Our results show a diverse variety of both new and previously observed flow patterns. These flow patterns emerge as a consequence of various bifurcations ranging from pitchfork, Hopf, and homoclinic bifurcations to bifurcations involving double zero eigenvalues.

Convection in an arbitrary geometry is quite complex, so researchers have focused on Rayleigh-Bénard convection wherein the convective flow is between two conducting parallel plates [1]. The fluid has kinematic viscosity ν , thermal diffusivity κ , and coefficient of volume expansion α . The top and bottom plates are separated by distance d , and they are maintained at temperatures T_2 and T_1 , respectively, with $T_1 > T_2$. The convective flow in RBC is characterized by the Rayleigh number $R = \alpha(T_1 - T_2)gd^3/\nu\kappa$, where g is the acceleration due to gravity, and the Prandtl number $P = \nu/\kappa$. Various instabilities, patterns, and chaos are observed for different ranges of R and P [1,6,13]. Transition to chaotic states through various routes have been reported in convection [14,15].

^(a) Present address: Kabi Sukanta Mahavidyalaya - Angus, Hooghly (WB), India.

^(b) E-mail: mkv@iitk.ac.in

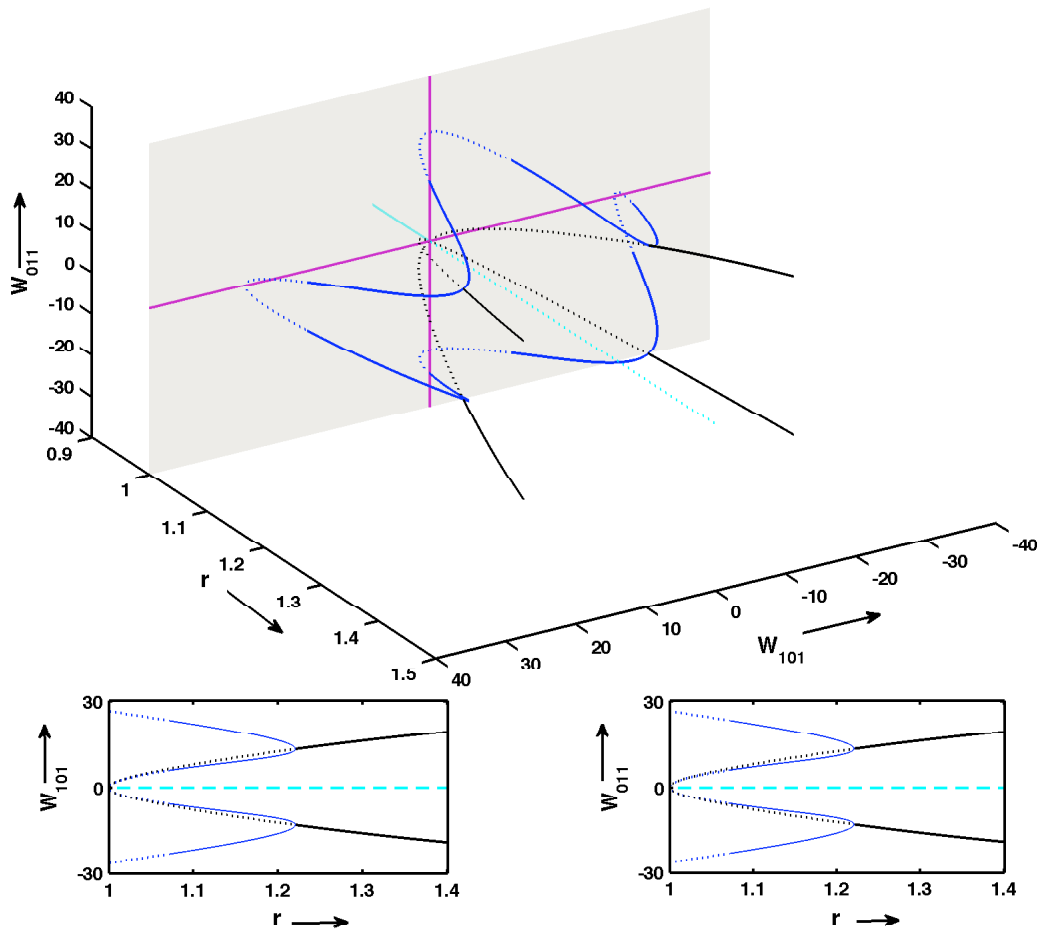


Fig. 1: (Colour on-line) Three-dimensional view of the bifurcation diagram showing the fixed points with solid and dashed curves representing the stable and unstable fixed points, respectively. Black, blue, and cyan curves represent stationary squares (SQ), asymmetric stationary squares (ASQ), and conduction state, respectively. All the points on the axis (purple lines) are 2D roll solutions. Below the 3D diagram we plot the values of W_{101} and W_{011} vs. r . These plots indicate xy symmetry in the system.

In this letter, we focus on zero-P convection. The governing zero-P Boussinesq equations [7] are nondimensionalized using d as length scale, d^2/ν as time scale, and $\nu(T_1 - T_2)/\kappa$ as temperature scale which yields

$$\partial_t(\nabla^2 v_3) = \nabla^4 v_3 + R \nabla_H^2 \theta - \hat{\mathbf{e}}_3 \cdot \nabla \times [(\boldsymbol{\omega} \cdot \nabla) \mathbf{v} - (\mathbf{v} \cdot \nabla) \boldsymbol{\omega}], \quad (1)$$

$$\partial_t \omega_3 = \nabla^2 \omega_3 + [(\boldsymbol{\omega} \cdot \nabla) v_3 - (\mathbf{v} \cdot \nabla) \omega_3], \quad (2)$$

$$\nabla^2 \theta = -v_3, \quad (3)$$

$$\nabla \cdot \mathbf{v} = 0, \quad (4)$$

where $\mathbf{v} \equiv (v_1, v_2, v_3)$ is the velocity field, θ is the deviation in the temperature field from the steady conduction profile, $\boldsymbol{\omega} = \nabla \times \mathbf{v}$ is the vorticity field, $\hat{\mathbf{e}}_3$ is the vertically directed unit vector, and $\nabla_H^2 = \partial_{xx} + \partial_{yy}$ is the horizontal Laplacian. We consider *perfectly conducting and free-slip boundary* conditions at the top and bottom plates, and periodic boundary conditions along the horizontal directions [6,15]. In the following discussion we also use the

reduced Rayleigh-number $r = R/R_c$, where R_c is the critical Rayleigh number.

Straight two-dimensional (2D) rolls that have zero vertical vorticity are neutrally stable solution of zero-P convection at $r=1$. However they become unstable for $r > 1$. Busse [9], Thual [6] and Kumar *et al.* [8] showed that these 2D rolls saturate through generation of vertical vorticity (wavy rolls) for $r > 1$ both for low-Prandtl-number and zero-P fluids. Thus vorticity plays a critical role in zero-P convection.

Herring [10] was first to simulate these equations under the free-slip boundary conditions. However he observed divergence of the solutions possibly due to the instabilities described above. The first successful simulation of zero-P equations with free-slip boundary conditions was done by Thual [6]. He reported many interesting flow patterns including relaxation oscillation of square patterns (SQOR) and stationary square patterns (SQ). Later Knobloch [11] studied the stability of the SQ patterns using amplitude equations. Pal and Kumar [12] explained the mechanism of selection of the square patterns using a 15-dimensional

Table 1: Range of reduced Rayleigh number r corresponding to various flow patterns observed in the model and the DNS. Here SQ, ASQ, OASQ, and SQOR represent stationary squares, stationary asymmetric squares, oscillatory asymmetric squares, and relaxation oscillation of squares, respectively.

Flow patterns	r (Model)	r (DNS)
Chaotic	1–1.0045	1–1.0048
SQOR	1.0045–1.0175	1.0048–1.0708
OASQ	1.0175–1.0703	1.0709–1.1315
ASQ	1.0703–1.2201	1.1316–1.2005
SQ	1.2201–1.4373	1.2006–1.4297

model. Note that the asymmetric squares (referred to as “cross roll” in literature) and other patterns have been observed in experiments of low-Prandtl-number convection [1,16].

We performed around 100 DNS runs of zero-P convection (eqs. (1)–(4)) using a pseudo-spectral code for various r values on 64^3 box. The aspect ratio of our simulation is $2\sqrt{2}:2\sqrt{2}:1$. In DNS we observe stationary squares (SQ), stationary asymmetric squares (ASQ), oscillatory asymmetric squares (OASQ), relaxation oscillations with squares (SQOR), and chaos.

For our bifurcation analysis we construct a low-dimensional model using the energetic modes of the above-mentioned simulation in the range of $r = 1 - 1.4$. We pick 9 large-scale vertical velocity modes (real Fourier amplitudes): W_{101} , W_{011} , W_{202} , W_{022} , W_{103} , W_{013} , W_{112} , W_{121} , W_{211} , and 4 large-scale vertical vorticity modes (real Fourier amplitudes): Z_{110} , Z_{112} , Z_{121} , Z_{211} . The three subscripts are the indices of wavenumber along x , y , and z directions. Cumulative energy contained in these modes ranges from 85% to 98% of the total energy of DNS, and each of these modes has 1% or more of the total energy. We derive the model equations by the Galerkin projection of eqs. (1)–(4) on the subspace of these modes. This results in thirteen coupled first-order ordinary differential equations for the above variables. The low-dimensional model captures all the flow patterns of DNS mentioned above. The range of r for these patterns for the model and DNS are shown in table 1, and they are reasonably close to each other. Interestingly, the stable steady values of the modes W_{101} , W_{011} , W_{112} , W_{121} , W_{211} for SQ and ASQ patterns match with corresponding DNS values within 10%.

The origin of the above flow patterns can be nicely understood using the bifurcation diagram of the low-dimensional model. To generate the bifurcation diagram, we first evaluate a fixed point numerically using the Newton-Raphson method for a given r . The branch of the fixed points is subsequently obtained using a fixed arc-length based continuation scheme [17]. Stability of the fixed points is ascertained through an eigenvalue analysis of the Jacobian and accordingly the bifurcation points are located. New branches of fixed points are born when

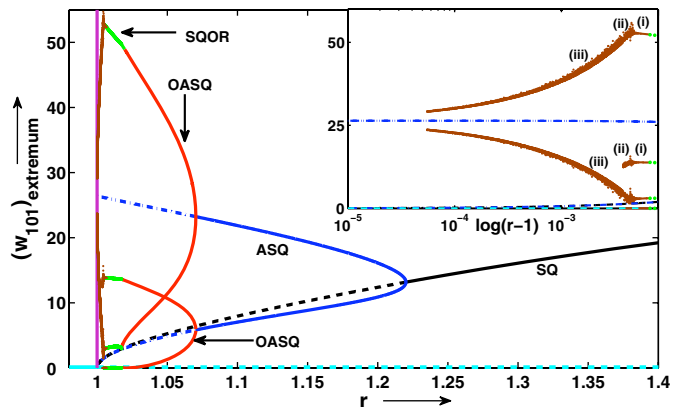


Fig. 2: (Colour on-line) Bifurcation diagram of the model for $0.95 \leq r \leq 1.4$. The stable branches corresponding to stationary squares (SQ) and stationary asymmetric squares (ASQ) are represented by solid black and solid blue lines, respectively. Red, green, and brown curves represent the extrema of oscillatory asymmetric squares (OASQ), relaxation oscillation of squares (SQOR), and chaotic solutions, respectively. A zoomed view of the bifurcation diagram for the chaotic regime is shown in the inset. In the inset, the x -axis is chosen as $\log(r-1)$ to highlight the behaviour near $r = 1$. Branches corresponding to the unstable fixed points are represented by dashed lines. Cyan line represents the conduction state.

the eigenvalue(s) become zero (pitchfork), and branches of periodic solutions appear when the eigenvalue(s) become purely imaginary (Hopf). Subsequent branches are generated by calculating and continuing the new steady solutions close to the bifurcation points.

Fixed points play an important role in the bifurcation analysis. The fixed points of the low-dimensional model are depicted in fig. 1 as projections onto the W_{101} and W_{011} modes. For clear visualization, the bottom of fig. 1 contains projections only on the individual modes. For $r < 1$, the origin is the unique stable fixed point corresponding to the pure conduction state. At $r = 1$, pure convective roll solutions (corresponding to the W_{101} or W_{011} axis of fig. 1) are neutrally stable. There is a double zero eigenvalue at $r = 1$ [18], and all the fixed points (13 in number) arising from $r = 1$ are unstable for $r > 1$. These fixed points are shown as dotted lines in fig. 1. Four of these branches of fixed points bifurcate from the origin; these fixed points satisfy $|W_{101}| = |W_{011}|$. The other 8 branches of unstable fixed points emerge from nonzero W_{101} or W_{011} , and they obey $|W_{101}| \neq |W_{011}|$ (see fig. 1). With an increase of r , these 8 branches become stable and merge with the 4 branches that originate from the origin.

After a discussion on the fixed points, we focus on the bifurcation diagram in the range $1 \leq r \leq 1.4$ (see fig. 2). Chaotic solutions are observed at the onset of convection itself, *i.e.*, just above $r = 1$. A better insight into the origin of the various solutions is facilitated by starting the analysis at a higher r value and tracking the various bifurcations while approaching $r = 1$.

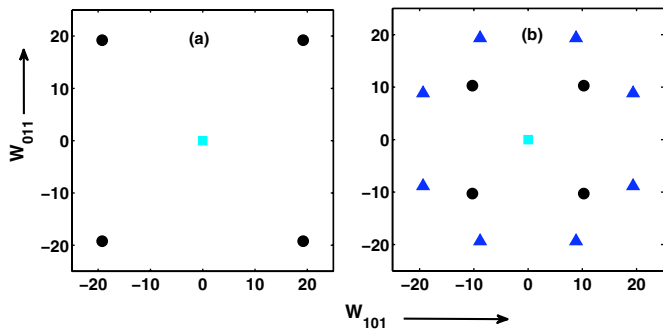


Fig. 3: (Colour on-line) Phase space projections of fixed points on the W_{101} - W_{011} plane for (a) $r = 1.4$ and (b) $r = 1.15$. The cyan square, black filled circles, and blue triangles represent the conduction fixed point, SQ fixed points, and ASQ fixed points, respectively.

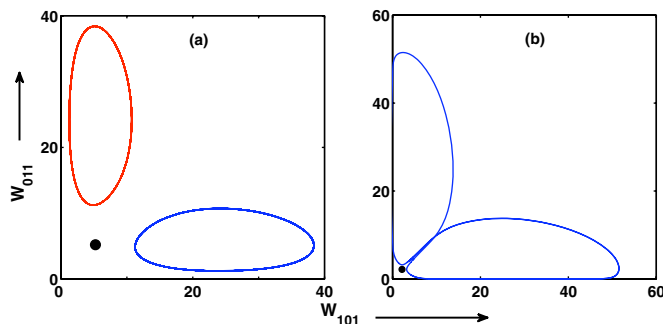


Fig. 4: (Colour on-line) Phase space projections of limit cycles on the W_{101} - W_{011} plane for (a) $r = 1.0494$ and (b) $r = 1.0099$. The limit cycles in (a) merge to form a single limit cycle in (b). Black dots indicate the symmetric square saddle.

We start our analysis at $r = 1.4$ where we observe stable symmetric squares (SQ) with $|W_{101}| = |W_{011}|$ corresponding to the black curve in fig. 1. The state-space projection on W_{101} - W_{011} plane for $r = 1.4$ is shown in fig. 3(a). In this figure SQ fixed points are represented by the filled circles. In fig. 2 we represent only the $W_{101} = W_{011}$ solution. As r is reduced from 1.4, the SQ branch of fixed points loses stability via a supercritical pitchfork bifurcation at $r \approx 1.2201$, after which we observe stationary solutions with $W_{101} \neq W_{011}$ (blue curves of figs. 1 and 2). These solutions correspond to asymmetric square patterns (ASQ), either dominant along the x axis ($|W_{101}| > |W_{011}|$), or dominant along the y axis ($|W_{101}| < |W_{011}|$). These states are represented by filled triangles in fig. 3(b) for $r = 1.15$. The SQ solution $|W_{101}| = |W_{011}|$ continues as a saddle. With a further reduction of r , ASQ branches lose stability through a supercritical Hopf bifurcation at $r \approx 1.0703$ and limit cycles are born. These limit cycles are represented by red curves in fig. 2. Physically they represent oscillatory asymmetric square patterns (OASQ). Figure 4(a) illustrates the projection of two of these stable limit cycles (for $r = 1.0494$) on the W_{101} - W_{011} plane.

The limit cycles grow in size as r is lowered. A homoclinic orbit is formed at $r \approx 1.0175$. Afterwards, homoclinic

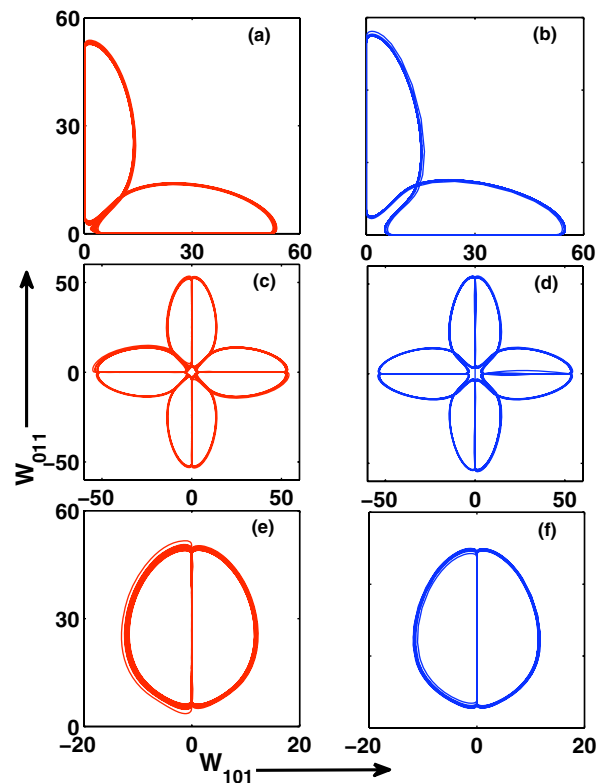


Fig. 5: (Colour on-line) The three different chaotic solutions observed near $r = 1$: Ch1 at $r = 1.0041$ for the model (a) and at $r = 1.0045$ in DNS (b); Ch2 at $r = 1.0038$ for the model (c) and at $r = 1.0030$ in DNS (d); Ch3 at $r = 1.0030$ for the model (e) and at $r = 1.0023$ in DNS (f). These solutions belong to (i), (ii), and (iii) regimes in the bifurcation diagram (fig. 2).

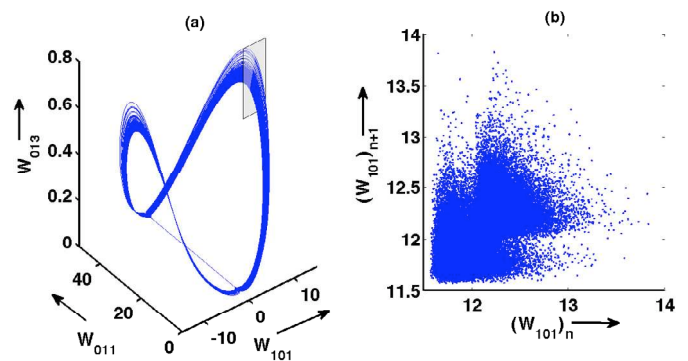


Fig. 6: (Colour on-line) (a) The three-dimensional projection of the Ch3 orbit on the $(W_{101}, W_{011}, W_{013})$ space for $r = 1.0030$. This solution belongs to the (ii) regime in the bifurcation diagram (fig. 2). (b) The first return map of the variable W_{011} on the Poincaré plane $W_{011} = 25$ shown in (a).

chaos is observed in a narrow window. At lower r the attractor becomes regular resulting in a larger limit cycle that corresponds to the relaxation oscillations with an intermediate square pattern (SQOR). Figure 4(b) illustrates the projection of this limit cycle at $r = 1.0099$. The flow pattern in this regime changes in time from

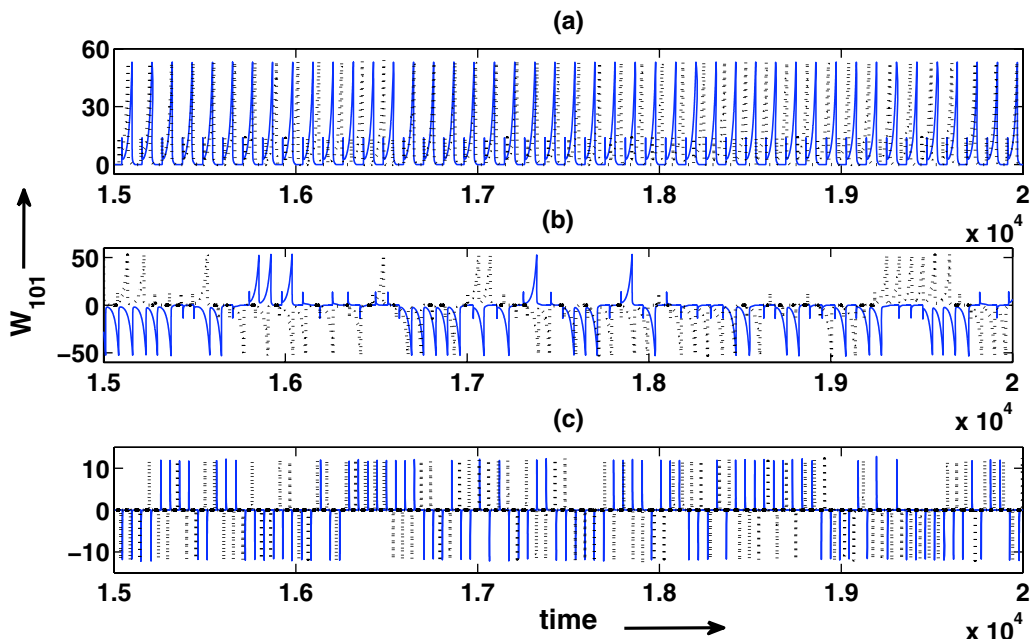


Fig. 7: (Colour on-line) For the model, the chaotic time series of the W_{101} mode for the Ch1 (a), Ch2 (b), and Ch3 (c) attractors for $r = 1.0041, 1.0038$ and 1.0030 . The two time series in each of the panels are generated using two initial conditions that differ from each other by $\Delta W_{101} = 10^{-6}$. The trajectories diverge from each other very quickly indicating chaotic nature of the attractor. In panels (b) and (c) (Ch2 and Ch3 attractors), the signal switches sign intermittently.

an approximate pure roll in one direction to a symmetric square, and then to an approximate pure roll in the perpendicular direction. The SQOR solution is represented by the green curve in fig. 2.

The flow becomes chaotic as $r \rightarrow 1$. The chaotic flow manifests itself in three different forms: Ch1, Ch2, and Ch3 as shown in the inset of fig. 2 as (i), (ii), and (iii), respectively. The phase space projection for these three solutions are depicted in fig. 5 for $r = 1.0041, 1.0038$ and 1.0030 for the 13-mode model, and for $r = 1.0045, 1.0032$ and 1.0023 in the DNS. A three-dimensional projection of the Ch3 attractor is shown in fig. 6(a). The first return map of W_{101} for the Poincaré plane $W_{011} = 25$ is shown in fig. 6(b). A scatter in this map indicates the chaotic nature of the attractor. We also observe these chaotic attractors in DNS albeit at different r values. The state space projections corresponding to DNS are shown in fig. 5(b), (d), (f).

In fig. 7 we plot the time series for the three types of chaotic attractors for the values of r given in fig. 5 using random initial conditions. In each subplot, the solid and dotted lines represent two time series generated using two initial conditions that differ by $\Delta W_{101} = 10^{-6}$. A clear divergence between the two solutions (sensitivity to initial conditions) shows that the attractors are chaotic. The power spectra of the above time series are broadband as shown in fig. 8. This result corroborates with the earlier conclusions on the chaotic nature of the attractor.

The time series for the W_{101} mode of the Ch1 attractor appears to be periodic visually, but the power spectra and the sensitivity to initial conditions indicate its chaotic

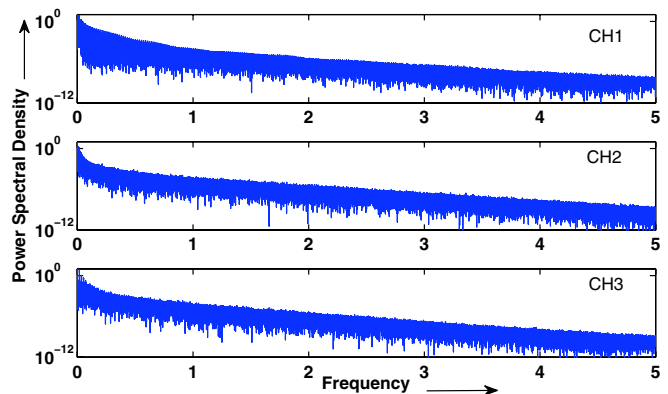


Fig. 8: (Colour on-line) The power spectral density obtained from the time signal of the W_{101} mode for the Ch1 ($r = 1.0041$), Ch2 ($r = 1.0038$), and Ch3 ($r = 1.0030$) regimes. They exhibit broadband indicating chaotic nature of the attractor.

nature. The Poincaré first return map of the attractor also shows scatter similar to that in Ch3 shown in fig. 6(b). In the second time series (for the Ch2 attractor), the modes W_{101} switches sign intermittently, which is due to the transit of the system from one quadrant to another in the state space projection shown in fig. 5. For the Ch3 attractor, the time series of the mode W_{101} has a very similar feature. The time series of the Ch2 and Ch3 attractors differ when we plot W_{011} as evident from state space plots of fig. 5.

We investigate the origin of the attractors Ch1, Ch2, and Ch3. The attractor Ch1 originates from homoclinic

chaos associated with the saddle corresponding to the dashed line originating from SQ. The attractor Ch1 however is quite thin, and its largest Lyapunov exponent is very small but positive. Note that there are four Ch1 attractors due to symmetry. As r is reduced, the four attractors collide simultaneously with their respective basin boundaries and yields a larger chaotic attractor Ch2 of fig. 5(c) [19]. This is the “attractor merging crisis”. The resulting dynamics is intermittent (crisis induced intermittency [19]), as exhibited by the time series (see fig. 7). As r is reduced further, another crisis occurs when the Ch2 attractor breaks into four small attractors Ch3 of fig. 5(e). Note that the nature of these three chaotic attractors are quite different. With a further reduction in the Rayleigh number, the size of these chaotic attractors decreases and they ultimately merge with one of the branches of the unstable ASQ fixed points at $r = 1$. In fig. 2, we exhibit the merger of one of these chaotic attractors with the unstable ASQ fixed point with $W_{101} \approx 26.4$.

In conclusion, we present for the first time a numerically obtained, DNS validated, detailed bifurcation diagram and associated flow structures of zero-P convective flow near the onset of convection. The whole spectrum of phenomena observed in DNS near the onset of convection is replicated by the low-dimensional model. Hence, the bifurcation structure presented here explains the origin and dynamics of various patterns near the onset of convection. Recent analysis of VKS (Von-Karman-Sodium) experimental results indicate a strong role of large-scale modes for the magnetic field reversal [20]. A study of large-scale modes as outlined in this letter may provide useful insights into the mechanism behind the generation and reversal of magnetic field. The dynamics of large-scale modes in other hydrodynamic systems like rotating turbulence, magneto-convection etc. could also be captured by a similar approach.

In this paper we have performed analysis for zero-P convection for $1 \leq r \leq 1.4$. The bifurcation analysis for $r > 1.4$ is reasonably complex, and it will be reported later. In addition, preliminary results show a reasonable amount of similarity between low-Prandtl-number convection and zero-P convection. These issues are under investigation.

We thank S. FAUVE, A. CHATTERJEE, A. K. MALLIK, and V. SUBRAHMANYAM for very fruitful discussions. We thank Computational Research Laboratory, India for providing us access to the supercomputer EKA where part of this work was done. We also thank the two anonymous referees for useful comments and suggestions. This work was supported by the research grant of Department of Science and Technology, India.

REFERENCES

- [1] CHANDRASEKHAR S., *Hydrodynamic and Hydromagnetic Stability* (Cambridge University Press, Cambridge) 1961; BUSSE F. H., in *Hydrodynamic Instabilities and the Transition to Turbulence*, edited by SWINNEY H. L. and GOLLUB J. P., *Top. Appl. Phys.*, Vol. **45** (Springer, Berlin) 1985, pp. 97–137; MANNEVILLE P., *Instabilities Chaos and Turbulence* (Imperial College Press, London) 2004; AHLERS G., GROSSMANN S. and LOHSE D., *Rev. Mod. Phys.*, **81** (2009) 503; BHATTACHARJEE J. K., *Convection and Chaos in Fluids* (World Scientific, Singapore) 1987.
- [2] STEIN R. F. and NORLUND A., *Sol. Phys.*, **192** (2000) 91; CATTANEO F., EMONET T. and WEISS N., *Astrophys. J.*, **588** (2003) 1183.
- [3] BUSSE F. H., in *Fundamentals of Thermal Convection Mantle Convection, Plate Tectonics and Global Dynamics*, edited by PELTIER W. R. (Gordon and Breach) 1989, pp. 23–95.
- [4] DAVIDSON P. A., *An Introduction to Magnetohydrodynamics* (Cambridge University Press, Cambridge) 2001.
- [5] PROCTOR M. R. E., *J. Fluid Mech.*, **82** (1977) 97; CLEVER R. M. and BUSSE F. H., *J. Fluid Mech.*, **102** (1981) 61; KEVREKIDIS I. G. *et al.*, *Physica D*, **71** (1994) 342; BODENSCHATZ E., PESCH W. and AHLERS G., *Annu. Rev. Fluid Mech.*, **32** (2000) 709.
- [6] THUAL O., *J. Fluid Mech.*, **240** (1992) 229.
- [7] SPIEGEL E. A., *J. Geophys. Res.*, **67** (1962) 3063.
- [8] KUMAR K., FAUVE S. and THUAL O., *J. Phys. II*, **6** (1996) 945; KUMAR K., Woods Hole Oceanogr. Inst. Tech. Rep. WHOI-90-01 (1990).
- [9] BUSSE F. H., *J. Fluid Mech.*, **52** (1972) 97.
- [10] HERRING J. R., Woods Hole Oceanogr. Inst. Tech. Rep. WHOI-70-01 (1970).
- [11] KNOBLOCH E., *J. Phys. II*, **2** (1992) 995.
- [12] PAL P. and KUMAR K., *Phys. Rev. E*, **65** (2002) 047302.
- [13] CROSS M. C. and HOHENBERG P. C., *Rev. Mod. Phys.*, **65** (1993) 851; HU Y. C., ECKE R. and AHLERS G., *Phys. Rev. Lett.*, **72** (1994) 2191; LIU J. and AHLERS G., *Phys. Rev. Lett.*, **77** (1996) 3126; EGOLF D. A. *et al.*, *Nature*, **404** (2000) 733; KUMAR K., CHAUDHURI S. and DAS A., *Phys. Rev. E*, **65** (2002) 026311.
- [14] MAURER J. and LIBCHABER A., *J. Phys. (Paris), Lett.*, **41** (1980) 515; BERGE P. *et al.*, *J. Phys. (Paris), Lett.*, **41** (1980) 341; GOLLUB J. P. and BENSON S. V., *J. Fluid Mech.*, **100** (1980) 449; GIGLIO M., MUSSAZI S. and PERINI V., *Phys. Rev. Lett.*, **47** (1981) 243; LIBCHABER A., LAROCHE C. and FAUVE S., *J. Phys. (Paris), Lett.*, **43** (1982) 211.
- [15] MENEGUZZI M. *et al.*, *J. Fluid Mech.*, **182** (1987) 169.
- [16] CROQUETTE V., *Contemp. Phys.*, **30** (1989) 113; 153.
- [17] NANDAKUMAR K. and CHATTERJEE A., *Nonlinear Dyn.*, **40** (2005) 143; WAHI P. and CHATTERJEE A., *Int. J. Nonlinear Mech.*, **43** (2008) 111.
- [18] GUCKENHEIMER J. and HOLMES P., *Nonlinear Oscillations Dynamical Systems, and Bifurcations of Vector Fields* (Springer, New York) 1983.
- [19] OTT E., *Chaos in Dynamical Systems* (Cambridge University Press, Cambridge) 2002.
- [20] PÉTRÉLIS F. *et al.*, *Phys. Rev. Lett.*, **102** (2009) 144503.